Journal of Sound and Vibration 329 (2010) 4380–4397

Contents lists available at ScienceDirect

Journal of Sound and Vibration

journal homepage: www.elsevier.com/locate/jsvi

Experimental and numerical investigation of the unsteady flow field and tone generation in an isolated centrifugal fan impeller

Daniel Wolfram [1], Thomas H. Carolus *

University of Siegen, Department of Fluid- and Thermodynamics, 57068 Siegen, Germany

ARTICLE INFO

Article history:
Received 6 November 2009
Received in revised form
20 April 2010
Accepted 28 April 2010
Handling Editor: P. Joseph
Available online 8 June 2010

ABSTRACT

In spite of a low circumferential Mach number the sound of isolated centrifugal fan impellers is sometimes dominated by distinctive tones at blade passing frequency (BPF) and integer multiples. This paper reports on an experimental and numerical investigation intended to unveil the tone generating mechanism. The sound spectra from three impellers operating at a large range of speed were measured and decomposed into Strouhal and Helmholtz number dependent functions. This led to the preliminary conclusion that the BPF related tones are exclusively flow-induced. Based on hot-wire and blade pressure fluctuation measurements and a subsequent correlation analysis, coherent flow structures different from those associated with the principal azimuthal flow pattern due to the blades were detected. Eventually a numerical three-dimensional unsteady flow simulation revealed an inlet vortex. It takes on a helical form, with the vortex core slowly varying its position with respect to the impeller center. As the blades cut through that quasi-stationary helical vortex they encounter blade force fluctuations, producing the BPF tones. Slow spin of the vortex core and slow variation of vortex strength were identified as the reasons for amplitude modulation of the BPF tone.

1. Introduction

Centrifugal fans are used for their ability to generate a relatively high total pressure rise at a reasonable compact size. Fig. 1 depicts various centrifugal fan assemblies with and without a volute, vaned radial diffusor at the outlet, adjustable guide vanes at the inlet, and an isolated impeller with just an inlet nozzle mounted in a wall separating pressure from suction side. Aiming at a high static pressure rise for many applications one can spare a volute or a vaned outlet diffusor if the impeller is designed for a high degree of reaction by selecting small blade angles and other appropriate dimensions. Typical applications of centrifugal fans consisting merely of an impeller and a stationary inlet nozzle are in heating–ventilating–air conditioning (HVAC) systems, cooling units in trains, ventilating systems for clean rooms, etc.

The noise generated in centrifugal fan impellers in general is both broadband and tonal. Broadband components are due to separated flow at the impeller shroud (i.e. at front plate of the closed impeller as the flow turns from the axial to the radial direction), turbulent and/or secondary flow in the blade channels, and flow/blade trailing edge interaction [1,2].

* Corresponding author. Tel.: +49 271 740 2386.
E-mail address: thomas.carolus@uni-siegen.de (T.H. Carolus).
[1] Current address: POLLRICH Ventilatoren GmbH, Neusser Str. 172, 41065 Mönchengladbach, Germany.

0022-460X/$ - see front matter © 2010 Elsevier Ltd. All rights reserved.
doi:10.1016/j.jsv.2010.04.034

Nomenclature

a	speed of sound
c	flow velocity in the stationary frame of reference (laboratory system)
b_1	impeller width at intake
b_2	impeller width at discharge
C, C_{xy}	coherence function
d_1	impeller intake diameter at blade leading edge
d_2	impeller diameter (at blade trailing edge)
F	function of Sr within spectral decomposition
G	function of He within spectral decomposition
He	Helmholtz number
l	chord length
L	level (in dB)
f	frequency
Ma	circumferential Mach number at d_2
m	azimuthal mode order
n	speed
p	static pressure, sound pressure
Re_d	Reynolds number based on d_2 and u_2
Sr	Strouhal number
t	time
u	circumferential velocity of impeller
$\dot{V}$	volume flow rate
w	flow velocity in the rotating frame of reference
W	sound power
z	number of blades
ζ_{xy}	phase angle between two signals x and y
η_{ts}	total to static efficiency
θ_{xy}	angular spacing angle of two probes x and y
λ	shaft power coefficient
ν	kinematic viscosity
ξ_{11}, ξ_{12}, ξ_3	blade coordinate system (rotating frame of reference)
φ_r	flow rate coefficient
ψ_{ts}	total to static pressure rise coefficient

Subscripts

0	reference value
1	at intake (leading edge)
2	at discharge (trailing edge)
Int	interaction
Mod	mode
opt	at design point
p	pressure
S	shaft
sp	surface pressure
W	sound power

Superscripts

$*$	non-dimensionalized

Abbreviations

BPF	blade passing frequency
CFD	computational fluid dynamics
LM100	100% size impeller
LM75	75% size impeller
LM50	50% size impeller
LE	leading edge
TE	trailing edge

Studies on rotating stall in centrifugal impellers resulting in tonal type noise are numerous. An early investigation was done by Gottschalk [3]. When the impeller is operated in the part load range the flow in one or more blade channels stalls and blocks off the flow in those channels. Through flow velocity in the remaining channels increases and ensures stall free flow. Those stall cells, however, are non-stationary with respect to their circumferential position in the impeller. They travel in the stationary frame of reference in the same direction as that of the impeller but with reduced speed. Mongeau et al. [4,5] investigated the sound generated by rotating stall in an impeller. They found that aerodynamic interaction between a rotating stall pattern and the blades dominates the low frequency noise production and is responsible for peaks in the acoustic signature. Among others they constructed the rotating flow field pattern from the signals of two stationary hot wire probes. Tetu et al. [6] identified two types of tones produced by the interaction of blades with modes of the coherent large scale instability: (i) a tone produced at the same frequency as an identified component of the large scale velocity field instability and (ii) tones at other frequencies generated by an interaction between the flow field fluctuating components at instability frequencies and the shaft rate frequency. Other works were done by Fringe and Van den Braembussche [7] and Pavesi et al. [8]. The typical frequency of rotating stall noise ranges from 60% to 80% of BPF but never equals BPF or its harmonics (Fig. 2).

In some cases a secondary flow between the stationary inlet nozzle and the impeller inlet creates a very dominant high frequency whistling sound (Fig. 3). This can be avoided by giving the nozzle–gap region a small asymmetric geometry, thus disturbing the flow slightly, see e.g. the utility model in Deutsches Gebrauchsmuster [11].

Isolated centrifugal impellers should not exhibit tonal noise at blade passage frequency (BPF) typically associated with the interaction between the periodic blade channel flow and guide vanes or the volute cuttoff. However, as manufacturers and customers report and as measurements confirm (Fig. 3), some designs may suffer from tonal noise at BPF. Simplistically these tones may be attributed to blade forces due to the flow deflection in the blade channel. Those forces are associated with change of angular momentum, the working principle of any turbomachine. The forces are stationary with respect to each rotating blade and form a rotating pressure field as they rotate. However, as shown by many authors, the sound radiated by those rotating forces is marginal as long as the circumferential Mach number (i.e. the circumferential speed at the impeller outlet over the speed of sound) of the impeller is far subsonic [12–16]. This is the case for most low pressure fans.

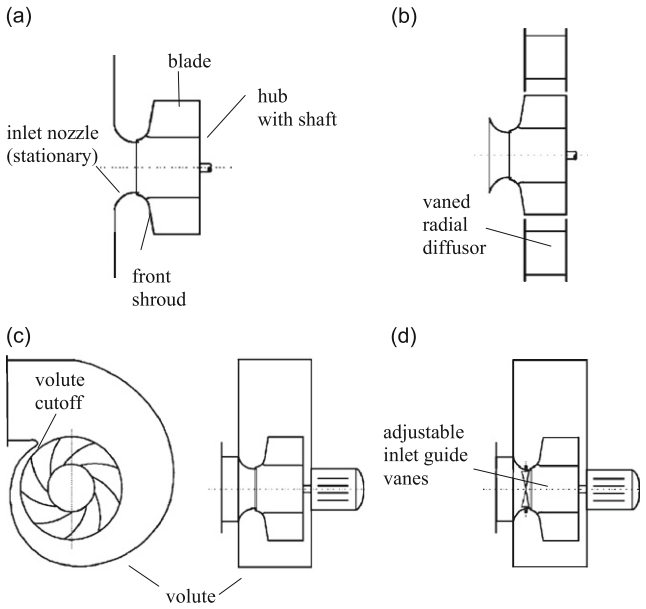

Fig. 1. Schematic view of various centrifugal fan assemblies: (a) isolated impeller with stationary inlet nozzle impeller, (b) impeller and vaned radial diffusor at outlet, (c) impeller with simple welded volute and (d) with adjustable inlet guide vanes.

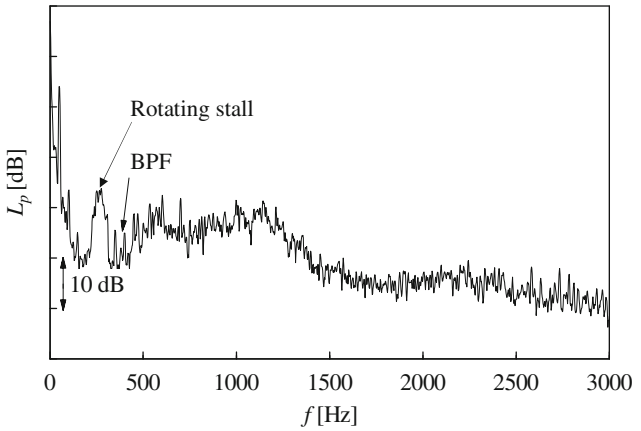

Fig. 2. Noise spectra of an isolated centrifugal impeller near design point; d_1/d_2=0.33, b_2/d_2=0.14, z=8, n=3000/min; rotating stall is responsible for the dominant tone [9].

To the knowledge of the authors, no work has been done on the noise at BPF from isolated centrifugal fan impellers. Thus the objective of this study is to characterize the noise in a controlled laboratory environment and eventually to shed some light on the noise generating mechanism.

2. Fans investigated and test rig

Three geometrically similar impellers, as depicted in Fig. 4 and specified in Table 1, have been built and investigated. Each of them has z=6 blades. The blades are swept backwards with a two-dimensional curvature. In order to avoid typical mass production tolerances the manufacturing process was controlled carefully. Hence the three impellers are nearly perfectly similar with respect to their geometry. Spark machining enabled even blade thickness to be scaled accurately.

The impeller takes air from a large semi-anechoic room via an inlet nozzle and exhausts into a pressure plenum with acoustically damped walls (Fig. 5). A duct with an anechoic termination is mounted on the chamber's pressure side. The operating point is controlled by a throttle downstream of the termination. The flow rate is measured by a hot film probe in the duct. The sound pressure is measured in the anechoic room by a calibrated microphone (Brühl and Kjaer type 4190) at r_s=1 m in front of the inlet nozzle on the axis of rotation. Sound power is calculated assuming sound pressure is equal on a

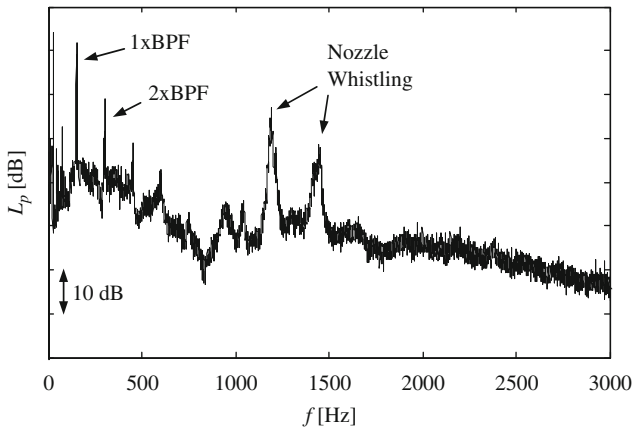

Fig. 3. Noise spectra of an isolated centrifugal impeller near design point; d_1/d_2=0.682, b_2/d_2=0.285, z=6, n=1500/min, dominant tones are at multiples of BPF and at high frequency due to nozzle whistling; note that the tones and the whistling are completely independent from each other [10].

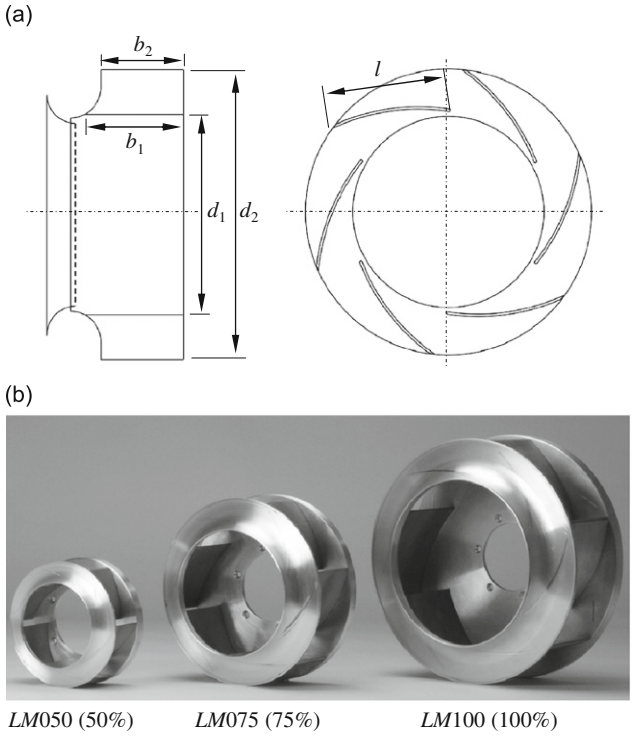

Fig. 4. (a) Impeller geometry and (b) the three geometrically similar impellers manufactured.

Table 1
Important impeller parameters.

		LM100	LM075	LM050
Intake diameter	d_1 [mm]	242	182	121
Impeller diameter	d_2 [mm]	355	266	178
Impeller width at d_1	b_1 [mm]	113	84	57
Impeller width at d_2	b_2 [mm]	101	76	51
Blade chord	l [mm]	150		

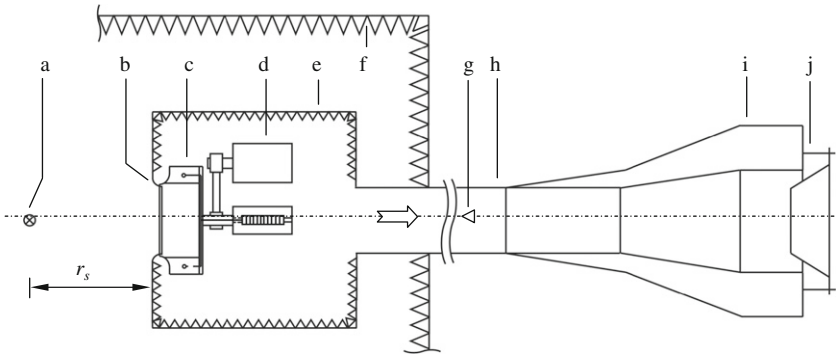

Fig. 5. Test rig; a, microphone; b, inlet nozzle; c, tested impeller; d, drive with belt transmission; e, pressure plenum; f, anechoic room; g, hot film probe; h, duct; i, anechoic termination; and j, adjustable throttle.

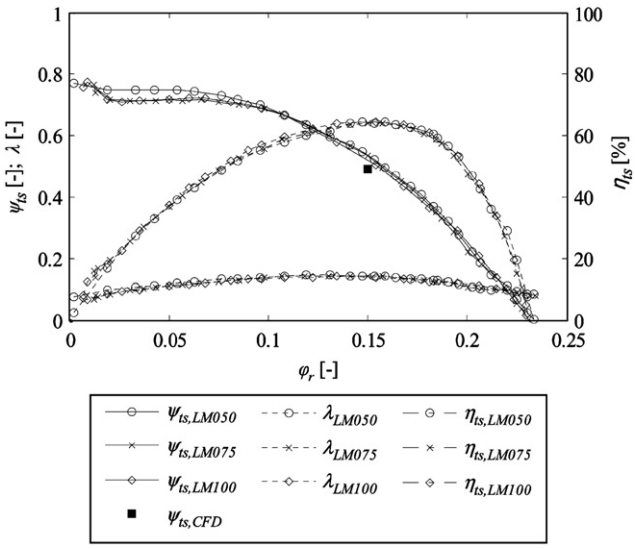

Fig. 6. Non-dimensional aerodynamic performance curves of the three impellers LM100, LM075, and LM050; ■ denotes a result from the numerical analysis in Section 6.

hemispherical surface surrounding the inlet. Although this simplification will not yield accurate sound power levels, it is thought to be sufficient for comparing acoustic effects within this study.

The reference pressure is $p_0=2\times10^{-5}$ Pa and reference sound power $W_0=10^{-12}$ W. The same value is taken as reference for the levels of surface pressure measurements in Sections 4 and 5.

All overall levels are the sum of narrow band levels from 50 Hz to 10 kHz. For the spectral analysis of all data MATLAB® routines (Version 7.0.4, R14) of The Mathworks Inc. are employed, e.g. power spectral density of an signal $x(t)$ is obtained with the routine pwelch with the parameter settings window=hann(nfft), noverlap=round(nfft/2) with nfft=round(T/8). If not otherwise stated, length of all measured time signals is T=30 s. Thus, we obtain a frequency resolution of $\Delta f=8/T=0.266$ Hz in all spectra.

3. Fan performance

3.1. Aerodynamic performance

The measured aerodynamic curves of operation are shown in Fig. 6. Note that unlike all other experiments the fans were mounted on a standard plenum test rig for fans according to the German standard DIN 24163 [17]. The following non-dimensional fan performance parameters are used:

- flow rate coefficient

$$\varphi_r=\frac{\dot{V}}{\pi^2 d_2^2 b_2 n}, \tag{1}$$

- total to static pressure rise coefficient

$$\psi_{\mathrm{ts}} = \frac{2\Delta p_{\mathrm{ts}}}{\pi^2 d_2^2 \rho n^2} \tag{2}$$

- shaft power coefficient

$$\lambda = \frac{8P_S}{\pi^4 d_2^5 \rho n^3}, \tag{3}$$

- total to static efficieny

$$\eta_{\mathrm{ts}} = \frac{\dot{V}\,\Delta p_{\mathrm{ts}}}{P_s}. \tag{4}$$

For the three impellers, speed was set individually to obtain the same value 4.37×10^5 of the Reynolds number

$$\mathrm{Re}_d = \frac{u_2 d_2}{\nu} = \frac{\pi n d_2^2}{\nu}. \tag{5}$$

The non-dimensional aerodynamic performance curves collapse nearly perfectly. Only the 50% impeller shows some small deviation at part load. For future reference the design point is defined as the point of operation with maximum total to static efficiency, i.e. at $\varphi_{r,\mathrm{opt}}$=0.15.

3.2. Acoustic performance

Fig. 7 shows the sound pressure time signal and part of the sound power spectrum in the vicinity of BPF as radiated from the 100% impeller at n=1000 rpm. The time signal reveals clearly the periodic fluctuations associated with BPF. Amplitude of the tone, however, varies more or less randomly with time. Taking instantaneous short interval spectra of the time signals it becomes obvious that sound pressure level varies by up to 15 dB within 30 s. This large scale amplitude modulation of the BPF tone is distinctly auditable. The time averaged spectrum within a larger frequency range is similar to the one shown in Fig. 3. In spite of this unsteadiness of sound production we will discuss time averaged spectra in the rest of the paper if not otherwise indicated.

In order to reveal fundamental characteristics of the radiated sound, sound power of these three impellers was determined for a range of rotational speeds from 500 up to 4000 rpm while varying the aerodynamic point of operation from partial load via the design point to overload. Subsequently the data have been evaluated in terms of non-dimensional parameters. The spectra have been further analyzed employing Weidemann's spectral decomposition technique [18,5].

The non-dimensional parameters employed have been derived from a standard dimensional analysis. Seven parameters are considered essential to describe the BPF tone problem: sound power W with its unit [W], speed of sound a [m/s], acoustic frequency f [Hz], volume flow rate $\dot{V}$ [m^3/s], rotational speed n [rpm], impeller diameter d_2 [m], and density of the fluid (here air) ρ [kg/m^3]. The acoustic frequency can be written in terms of the acoustic wave length λ as $f=a/\lambda$. In addition the (dimensionless) number of impeller blades z is added to the list. Possible effects of air viscosity and thus friction effects are neglected. Eventually one obtains four independent non-dimensional parameters as summarized in Table 2. The Strouhal number is defined such that Sr=1 corresponds to BPF, 2 to 2BPF, etc. Note that the Helmholtz number is not an

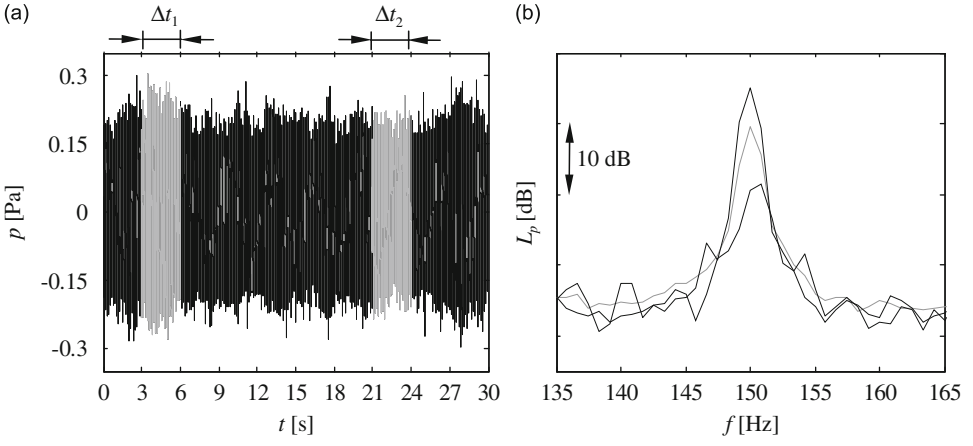

Fig. 7. Sound pressure at distance r_s from impeller LM100 operating at design point: (a) time signal of measured sound pressure and (b) time averaged sound pressure spectra of the entire interval (——) and instantaneous short interval spectra for Δt_1 (—) and Δt_2 (- - -).

independent parameter but arises from a combination of Strouhal and Mach numbers. The Helmholtz number is valuable for the forthcoming discussion.

The non-dimensional sound power spectra are decomposed in the form of product of two non-dimensional functions F and G, each being only a function of the Strouhal or the Helmholtz number, respectively:

$$W^* = F^2(\mathrm{Sr})G^2(\mathrm{He}), \tag{10a}$$

or in terms of a level

$$L_{W^*} = 10\log F^2(\mathrm{Sr}) + 10\log G^2(\mathrm{He})\,\mathrm{dB}. \tag{10b}$$

A Strouhal number dependency is characteristic for flow induced sound sources, whereas a Helmholtz dependency indicates effects of resonance and propagation.

Table 2
Non-dimensional parameters.

Normalized sound power	$W^* = W/d_2^5 n^3 \rho$, $L_{W^*} = 10\log W^*$ [dB]	(6)
Circumferential Mach number	$\mathrm{Ma} = u_2/a = \pi d_2 n/a$	(7)
Flow coefficient for centrifugal fans	$\varphi_r = \dot{V}/\pi^2 d_2^2 b_2 n$	(1)
Strouhal number	$\mathrm{Sr} = f/nz = f/\mathrm{BPF}$	(8)
Helmholtz number	$\mathrm{He} = \mathrm{Sr}\,\mathrm{Ma}(z/\pi) = d_2/\lambda = d_2 f/a$	(9)

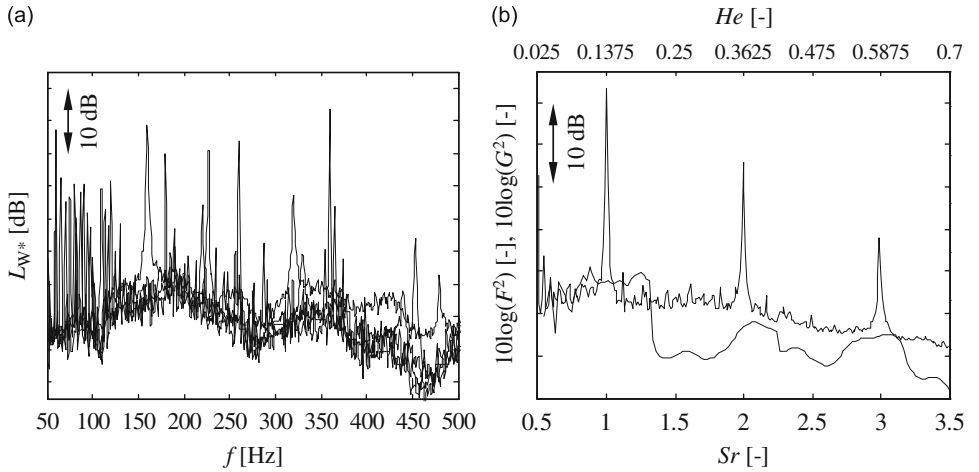

Fig. 8. Spectral decomposition of measured sound power spectra from the three to-scale centrifugal impellers at design point $\varphi_{r,\mathrm{opt}}$=0.15 at various rotational speeds: (a) non-dimensional power spectra and (b) squared functions F(Sr) (—) and G(He) (- - -).

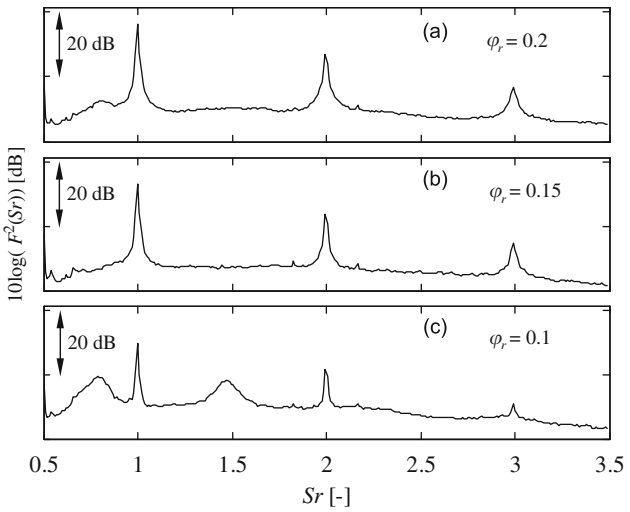

Fig. 9. F(Sr) function of impeller LM100 operating at (a) overload, (b) design point, and (c) part load.

Fig. 8a contains all measured and non-dimensionalized spectra $L_{W*}(f)$ from all three impellers at their design point $\varphi_{r,opt}=0.15$ at various rotational speeds. The decomposition, Fig. 8b, clearly reveals that (i) a decomposition according to Eq. (10) works and (ii) tones at BPF and their higher harmonics are a function of Strouhal but not of Helmholtz number. This leads to the conclusion that the BPF related tones are exclusively flow-induced. There is no evidence of a resonance phenomenon as a Helmholtz number dependency would indicate. Surprisingly, unlike phenomena such as rotating stall or nozzle whistling, levels of the BPF tones are nearly independent of the fan aerodynamic point of operation (Fig. 9).

4. Modal analysis

The previous results led to the hypothesis that a so far unidentified secondary flow structure exists, which interacts with the rotating impeller blades and causes fluctuating blade forces acting as an acoustic dipole source. This hypothesis is checked by a modal analysis of the near-blade flow field. A similar procedure, though applied to a different sound phenomenon, had been described by Bent [19] and Tetu et al. [20], see also Bendat and Piersol [21].

4.1. Theoretical background

Coherent secondary flow structures at the inflow and/or the discharge of a centrifugal impeller can be thought of as wave patterns along the circumference, so-called azimuthal modes. These modes may interact with the principal flow pattern associated with the blade channels rotating at rotor speed n. If the rotational speed of the modal wave pattern n_{Mod} differs from n, interactions occur every time a wave peak hits a blade edge. A special case is a steady mode, i.e. non-rotating in the stationary frame of reference.

An azimuthal mode and its interaction are characterized by three parameters: rotational speed of the wave pattern n_{Mod}, mode order m, i.e. number of waves along the impeller's circumference, and frequency of blade–mode interaction f_{Int}, which eventually may correspond to frequency of an acoustic tone radiated. Fig. 10 illustrates an arbitrary example. Since the impeller has six blade channels the principal flow pattern – rotating with the impeller's rotational speed n – is of 6th order, i.e. it has six lobes. The anticipated secondary flow structure has the shape of an azimuthal mode of order $m=5$, hence five lobes. It rotates with the so far unknown rotational speed n_{Mod}.

Detecting and characterizing azimuthal modes requires at least two signals $x(t)$ and $y(t)$ of a flow field variable, measured synchronously at different circumferential positions spaced at a known angular distance θ_{xy} apart.

The analysis used here is in the frequency domain. First, power spectral densities $S_{xx}(f)$, $S_{yy}(f)$ and cross-power spectral density $S_{xy}(f)$ are determined from the time signals. Since azimuthal modes are assumed to be coherent flow structures a large value of coherence function

$$C_{xy}(f)=\frac{|S_{xy}(f)|^2}{S_{xx}(f)S_{yy}(f)} \tag{11}$$

serves as an indicator (the coherence function varies from 0 to 1). Then the ratio of imaginary to real part of cross power spectral density yields the phase angle between both signals:

$$\zeta_{xy}=\arctan\left(\frac{\mathrm{Im}\{S_{xy}\}}{\mathrm{Re}\{S_{xy}\}}\right). \tag{12}$$

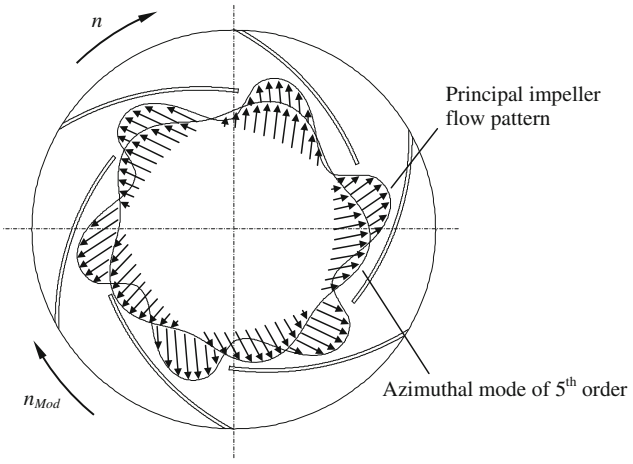

Fig. 10. Example: a fifth order mode interfering with the sixth order principal flow pattern at the inflow of a centrifugal impeller (schematically).

Since phase angle is bounded at $\pm 180^\circ$ the effective phase angle may differ from the measured one by an integer multiple of 360°. Eventually mode order is derived from phase angle and circumferential angle between the two data acquisition points as

$$m = \frac{\zeta_{xy}}{\theta_{xy}}. \tag{13}$$

Rotational speed of the azimuthal mode, measured by stationary probes, then becomes

$$n_{\mathrm{Mod}} = \frac{f}{m} = n\left(\frac{\mathrm{Sr}z}{m}\right), \tag{14}$$

whereas that measured by probes rotating with the impeller is

$$n_{\mathrm{Mod}} = n - \frac{f}{m} = n\left(1 - \frac{\mathrm{Sr}z}{m}\right). \tag{15}$$

Eqs. (14) and (15) require n_{Mod} to be a positive fraction of n. As a mode travels along one impeller circumference each of the m lobes interacts one time with each blade, i.e. the total number of interactions is

$$N_{\mathrm{Int,total}} = mz. \tag{16}$$

However, some lobes and blades may interact simultaneously and hence do not contribute to the acoustically relevant frequency of interaction. The number of mode–blade interactions, N_{Int}, which does not contain multiple interactions, can be found via a simple select and count routine. Eventually, both the number of those interactions and the mode's rotational speed yield the acoustically relevant frequency of mode–blade interaction:

$$f_{\mathrm{Int}} = N_{\mathrm{Int}}(n - n_{\mathrm{Mod}}). \tag{17}$$

Corresponding to the definition of the Strouhal number a non-dimensional frequency of interaction is defined as

$$f^*_{\mathrm{Int}} = \frac{f_{\mathrm{Int}}}{\mathrm{BPF}}. \tag{18}$$

Ambiguity of the result may be reduced by analyzing the unsteady flow field with more than just one pair of sensors.

Note that modes can be discovered only when they move relative to the probes. Hence probes in the stationary laboratory system are unable to detect modes that are stationary in the laboratory system. By contrast, probes fixed to the rotating impeller system cannot detect modes that rotate at the same speed as the impeller.

4.2. Instrumentation

Each impeller blade of the 100% impeller has been instrumented with seven flash mounted miniature pressure transducers (Knowles Acoustics type FG-3329-P07; Fig. 11); ξ_3 is the chordwise coordinate normalized with chord length, ξ_{11} and ξ_{12} are the spanwise coordinates normalized with rotor width at intake and discharge, respectively. The pressure transducers have been calibrated in situ. A slip ring transducer transfers the signals from the rotating impeller system to the non-rotating laboratory system. Both the random noise from the slip ring transducer and acceleration of the transducers due to the rotary motion are found to be negligible. Signals from three pairs of transducers at angular spacings θ_{xy}=60°, θ_{yz}=180°, and θ_{xz}=240°, inevitably given by the blade spacing, have been acquired simultaneously.

The unsteady inflow velocity to the impeller blade is measured by three stationary one-dimensional hot wire probes (Dantec Dynamics type 55P15/55H20; Fig. 12). The probes are mounted from the back of the intake through the hollow rotating shaft and the hub in order to not disturb the inflow. Their angular spacings are set to 30°, 45°, and 75°. The three probes can be traversed en bloc in the axial direction. Although the direction of the flow at the probes' location is not known a priori the wires are oriented normal to the circumferential direction. Expected inaccuracy in absolute velocity readings due to the potential misalignment is not decisive, since it will have minor effect on the space–time correlation the measurements are aimed at. A similar arrangement of hot wire probes is applied to the impeller discharge [22]. The hot wire signals are captured synchronously by a standard multi-channel constant-temperature anemometer system (Dantec CTA StreamLine) in connection with an appropriate data acquisition system.

In addition, the acoustic signal from the microphone as in Fig. 5 has been recorded synchronously. For the interpretation of the results it is important to know that the impeller speed was always set to 1500 rpm=25 Hz. The fan was always operated at its design point $\varphi_{r,\mathrm{opt}}$=0.15.

4.3. Results

By evaluating measured time records from pairs of stationary hot-wire and rotating blade surface pressure transducers one obtains coherence and phase data as shown in Fig. 13. The coherence function indicates consistent high coherence at discrete values of Sr. The values depend on whether the data originate from a stationary or rotating set of probes. High coherence is taken as an indicator for the existence of an azimuthal mode.

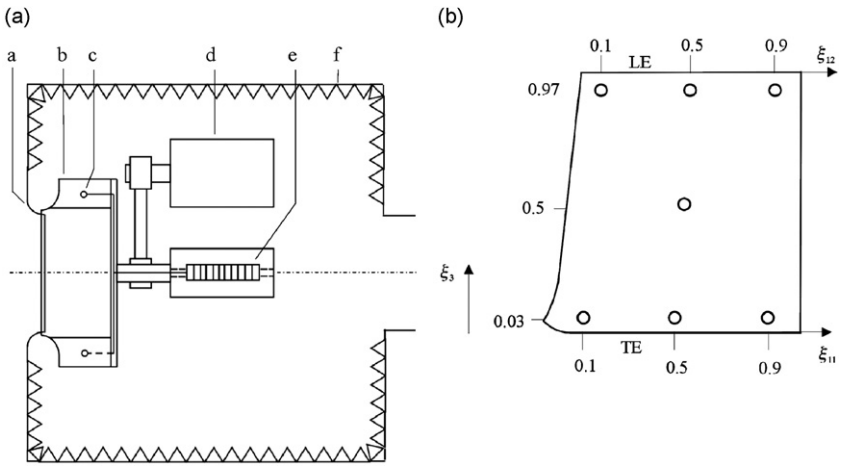

Fig. 11. Experimental set-up for blade pressure measurements: (a) *a*, stationary inlet nozzle; *b*, impeller; *c*, blade pressure sensor; *d*, drive; *e*, slip ring signal transducer; and *f*, pressure plenum; and (b) locations of flash mounted miniature pressure transducers on the blade surface.

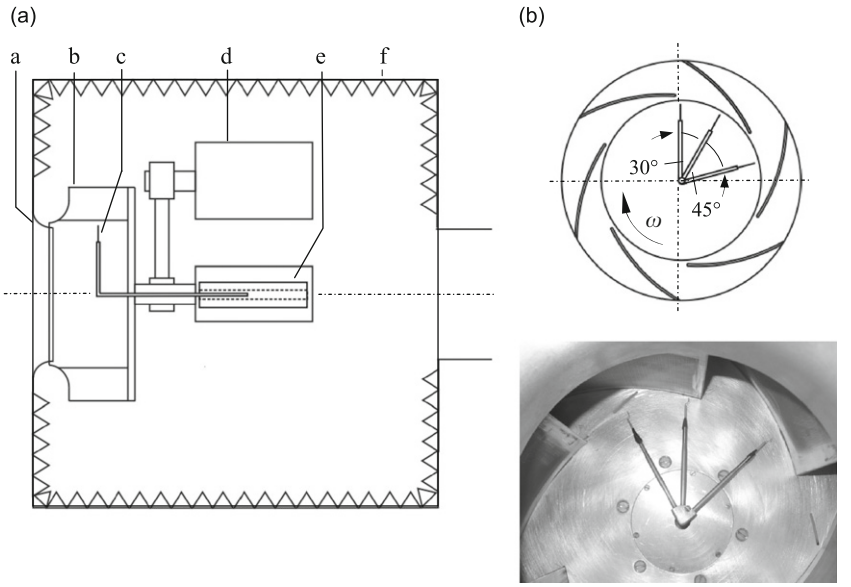

Fig. 12. Details of the experimental set-up for hot wire inflow velocity measurements: (a) *a*, stationary inlet nozzle; *b*, impeller; *c*, hot wire probe; *d*, drive; *e*, hollow shaft with probe traverse system; and *f*, pressure plenum; and (b) locations of the hot wire probes; note that the probes are stationary in the laboratory system.

Further evaluation reveals mode orders and their rotational speed as shown in Fig. 14. Clearly there exist modes of order 1 to at least 12. They either travel (i.e. rotate) with the same speed as the impeller or they are nearly stationary with respect to the laboratory system. The rotating modes are obtained from the stationary hot-wire probes. As pointed out earlier, modes traveling with the impeller speed $n_{\mathrm{Mod}}=n=1500$ rpm cannot interact with the principal flow and hence are not candidates for acoustic sources. Here they represent merely the principal flow pattern in the impeller. On the other hand, the stationary modes ($n_{\mathrm{Mod}}=0$ rpm), as detected by the rotating pressure probes, may well interact with the blade.

Fig. 15b indicates the number of mode–blade interactions detected while evaluating the 30 s time records. Most frequently an interaction is encountered at $f^*_{\mathrm{int}}=\mathrm{Sr}=1$. This nicely coincides with the tone produced at Sr=1 (i.e. at BPF) in the acoustic spectrum (Fig. 15a). Less frequently but still pronounced interactions exist at higher harmonics. Fig. 15c proves that coherence of the underlying pairs of signals is nearly perfect at those values of Sr. The associated azimuthal modes are the ones that do not rotate ($n_{\mathrm{Mod}}=0$ rpm, see Fig. 14). By contrast the modes detected as rotating with 1500 rpm yield frequencies of interaction $f^*_{\mathrm{Int}}=\mathrm{Sr}=0.9,\ 3.8,\ \text{and}\ 4.8$. Coherence of the underlying signals is remarkably lower and, as one might expect, their contribution in the sound power spectrum is negligible or non-existent.

The results so far are based on measurements from the impeller intake region. Although not shown here similar results have been obtained by analyzing data from the discharge region. In principle the modal analysis is not able to identify any

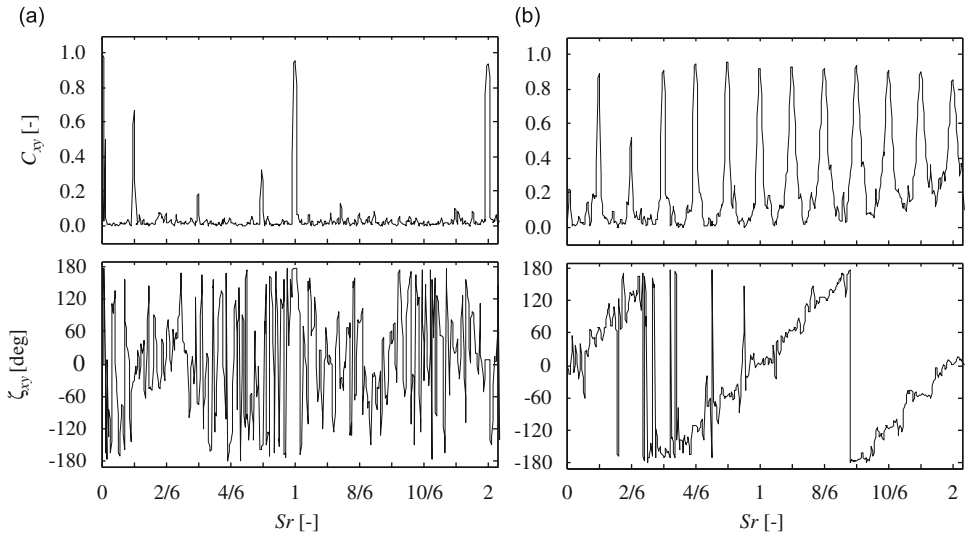

Fig. 13. Example: coherence and phase data at the intake (a) from a pair of stationary hot-wire probes and (b) a pair of blade surface pressure transducers.

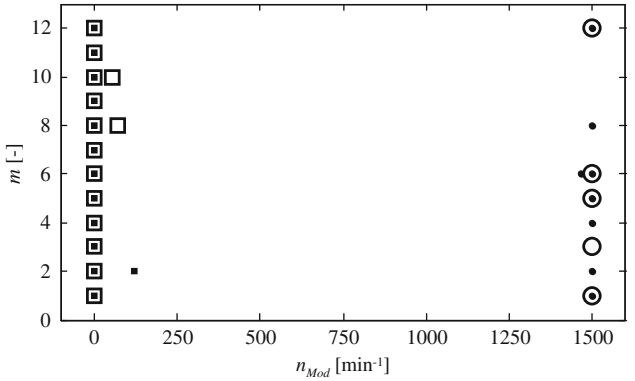

Fig. 14. Detected azimuthal modes: order m and mode rotational speed n_{Mod}; originating from velocity at intake ○, at discharge ●, pressure at intake □, at discharge ■.

causality. The azimuthal modes may be caused by flow structures either at the intake or the discharge or even within the blade channels. Fig. 16 shows pressure levels at various locations on the blade surface (cf. Fig. 11b). Evidently pressure peaks at the leading edge are 5–20 dB higher as compared to the trailing edge (i.e. at the discharge region). Likewise the highest surface pressure levels are found close to the hub, where the axial inflow impinges. This leads to the suspicion that the coherent flow structures are predominant in the intake. Correlation of pressure sensor signals in the chordwise direction from the leading to the trailing edge supports this hypothesis (Fig. 17). Coherent structures of a large range of Sr number (i.e. length scales) are convected with a constant velocity

$$c_c = \frac{-2\pi f l_{xy}}{\zeta_{xy}}, \tag{19}$$

where l_{xy} is the spacing between the two sensors. Numerical evaluation of convection speed gives values that coincide well with through flow velocity as simply obtained from blade channel cross sectional area and volume flow rate.

The overall conclusions from the modal analysis and the extended signal correlation are: (i) coherent flow structures exist; (ii) presumably they originate in the intake and are convected through the blade channels to the discharge of the impeller; (iii) they are steady or at least quasi-stationary with respect to the laboratory system; and (iv) they interact with the rotating blades and cause periodic blade force fluctuations that exactly match frequency of the radiated tones, namely BPF and its higher harmonics.

At first there is no thought on the existence of these flow structures. The inlet nozzle and the radial gap between nozzle and the impeller front shroud are kept symmetric to a high degree of accuracy, and inlet guide vanes do not exist.

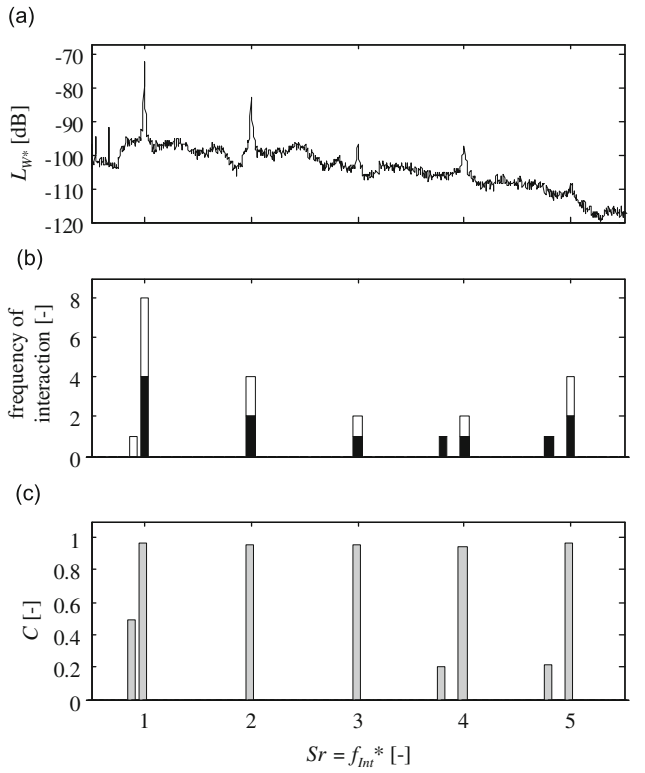

Fig. 15. Azimuthal modes as possible sound sources: (a) measured normalized sound power spectrum; (b) frequency of interaction due to mode–blade interaction at inflow (black bars) and discharge (white bars); and (c) coherence values.

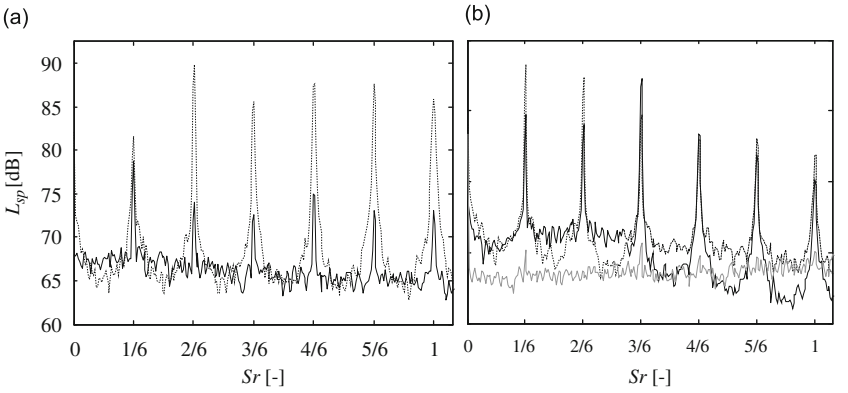

Fig. 16. Measured distribution of blade pressure fluctuations: (a) in chordwise direction at ξ_3=0.03 (i.e. at the leading edge; - - -) and ξ_3=0.97 (i.e. at the trailing edge; —) at ξ_{11}=ξ_{12}=0.5 and (b) in the axial direction along the leading edge at ξ_{11}=0.1 (——), ξ_{11}=0.5 (—), and ξ_{11}=0.9 (- - -).

Therefore, the impeller operates under extreme spatially uniform inflow conditions. Thus, a thorough understanding of the phenomenon requires unveiling the flow structures in more detail. This is done by a numerical analysis of the unsteady flow in the impeller.

5. Numerical analysis

5.1. Code and set-up

A three-dimensional (3D) unsteady numerical simulation of the flow through the impeller was performed. The hybrid scale adaptive simulation (SAS) method was selected. The SAS is a modified detached eddy simulation (DES) method that

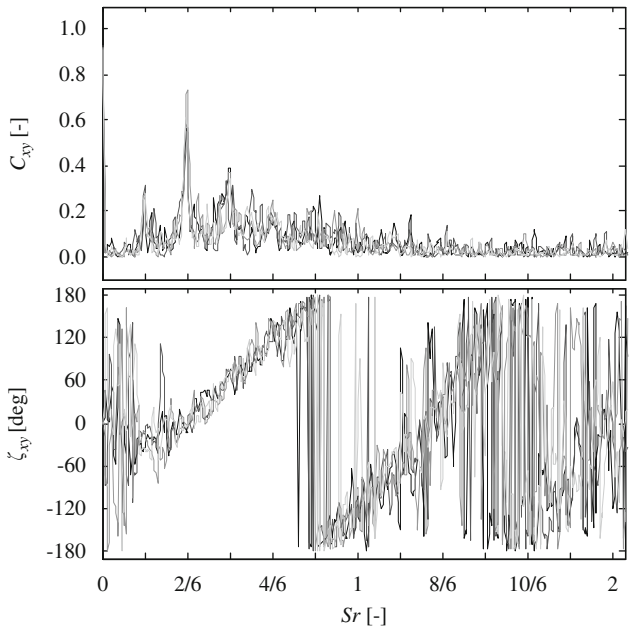

Fig. 17. Convection of coherent flow structures: coherence and phase data from measured blade pressure fluctuations between intake and discharge.

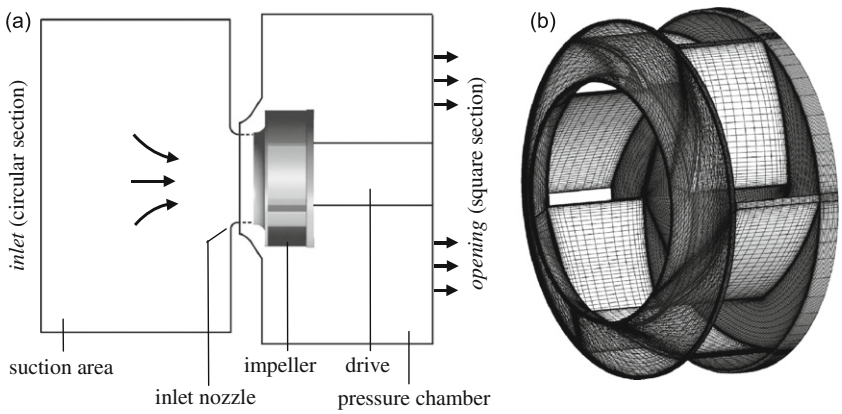

Fig. 18. Numerical simulation: (a) computational domain and (b) selected lines of the numerical grid.

provides a large eddy simulation (LES)-like behaviour in detached flows. The turbulence model used is the shear–stress-transport (SST) model. Unsteady parts of the flow field are solved with a second-order central difference scheme; otherwise a second-order upwind scheme with numerical advection correction is used. Time integration is done by a second-order backward Euler scheme. A detailed description of the SAS is given in [23,24]. The scheme is implemented in the commercial flow solver ANSYS CFX® 11.0, which is used throughout this study.

The computational domain is a simplified representation of the test rig (Fig. 18). The numerical grid consists of 1.64 million hexahedron elements.

The computational domain is divided into three domains: the non-rotating inlet, the rotating impeller, and the non-rotating outlet. All surfaces between rotating and non-rotating domains are connected via interfaces. At the inlet, mass flow rate is specified in terms of density and flow velocity normal to the surface such that the impeller operates at its design point, i.e. at $\varphi_{r,\mathrm{opt}}=0.15$. Also a medium degree of turbulence has been selected at the inlet. The cylindrical boundary of the large inlet-domain, the inlet nozzle, all wetted impeller surfaces, and boundaries of the pressure chamber, including walls of the simplified drive, are modelled as no slip walls. The fluid leaves the system at the outlet of the pressure chamber, where an opening boundary condition with static pressure set to 0 Pa has been specified. Time increment is set such that 2273 time steps correspond to one revolution of the impeller. Because of the CPU time required the simulation was limited to 11,365 time steps, resulting in a total simulation time of 0.2273 s or five revolutions of the impeller.

5.2. Numerical results

Fig. 19a shows an instantaneous picture of streamlines far upstream of the impeller intake. Time instances referred to are summarized in Table 3. Flow velocity increases gradually along the streamlines. Isosurfaces of velocity are nearly hemispheres. This proves that the inflow is symmetric and undisturbed. However, as the flow enters the impeller intake, gradually a pre-swirl is imposed on the inflow (Fig. 19b). In the centre region the streamlines begin to curl. Further light is

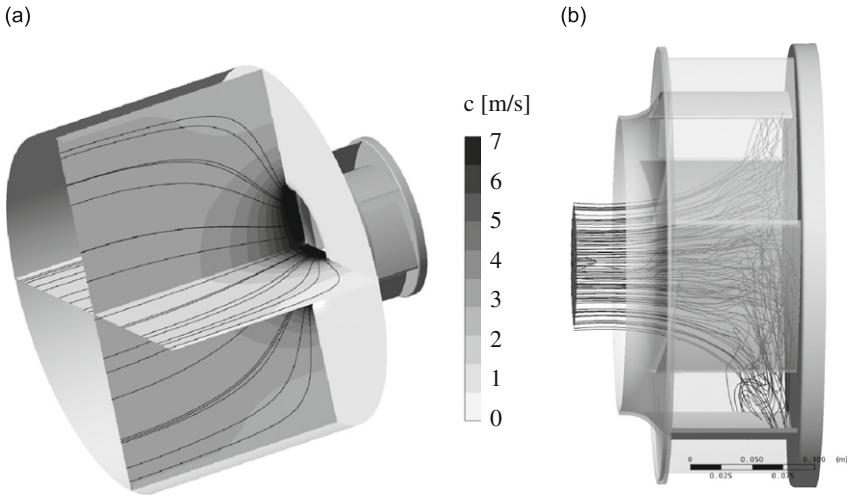

Fig. 19. Instantaneous streamlines at t_4: (a) downstream of the impeller intake and (b) in the centre region of the impeller intake.

Table 3
Time instances and angular impeller position for numerical data analysis.

Time instance	Time increment [10^{-3} s]	Angular impeller position [deg]
t_1	0	0
t_2	6.77	60
t_3	11.7	105
t_4	16.7	150
t_5	21.7	195
t_6	56.7	510

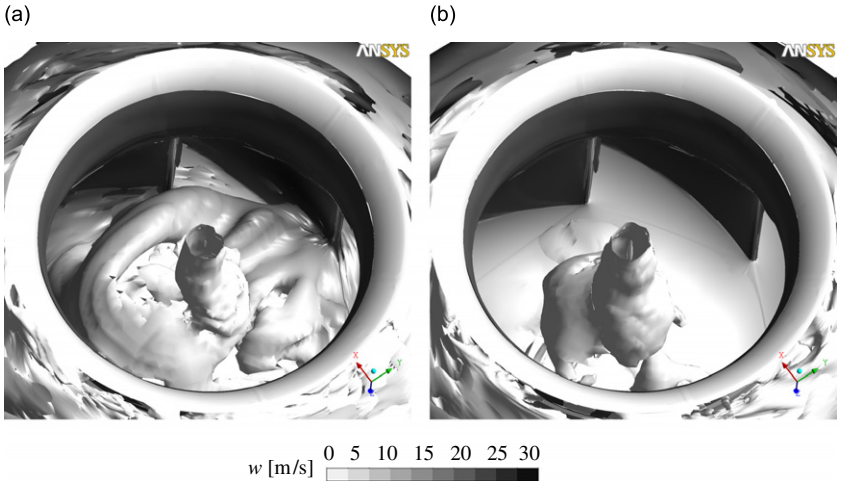

Fig. 20. Isovorticity surface at the impeller intake (500 s^{-1}, scaled with relative flow velocity) at time instance (a) t_1 and (b) t_6.

shed on the intake flow structure by visualization of isovorticy surfaces. Fig. 20 unveils clearly a helical vortex in the intake. Furthermore, the vortex core varies its position with time. Fig. 21 shows a time series of the instantaneous flow field close to the hub. The streamlines at t_3, t_4, and t_5 indicate that the eccentric position of the vortex core in the absolute frame of reference remains nearly constant while the impeller turns by 90°. At t_6 the vortex core has moved back to the centre. Thus the vortex core is not stationary but its movement is comparably slow as compared with impeller speed. The unsteady non-uniform velocity distribution is reflected in the pressure distribution as well (Fig. 21b). The vector field of velocity in the stationary laboratory system of reference, Fig. 21c, reveals even small vortices close to the hub. Strength of the intake vortex develops gradually from the front shroud to the hub as indicated from several cuts along the axial direction in Fig. 22. Of further interest are frequencies associated with the vortex and its spin. In Fig. 23 the predicted blade pressure fluctuation at a monitored point on the blade is compared with a measured time signal. The dominant frequency compares

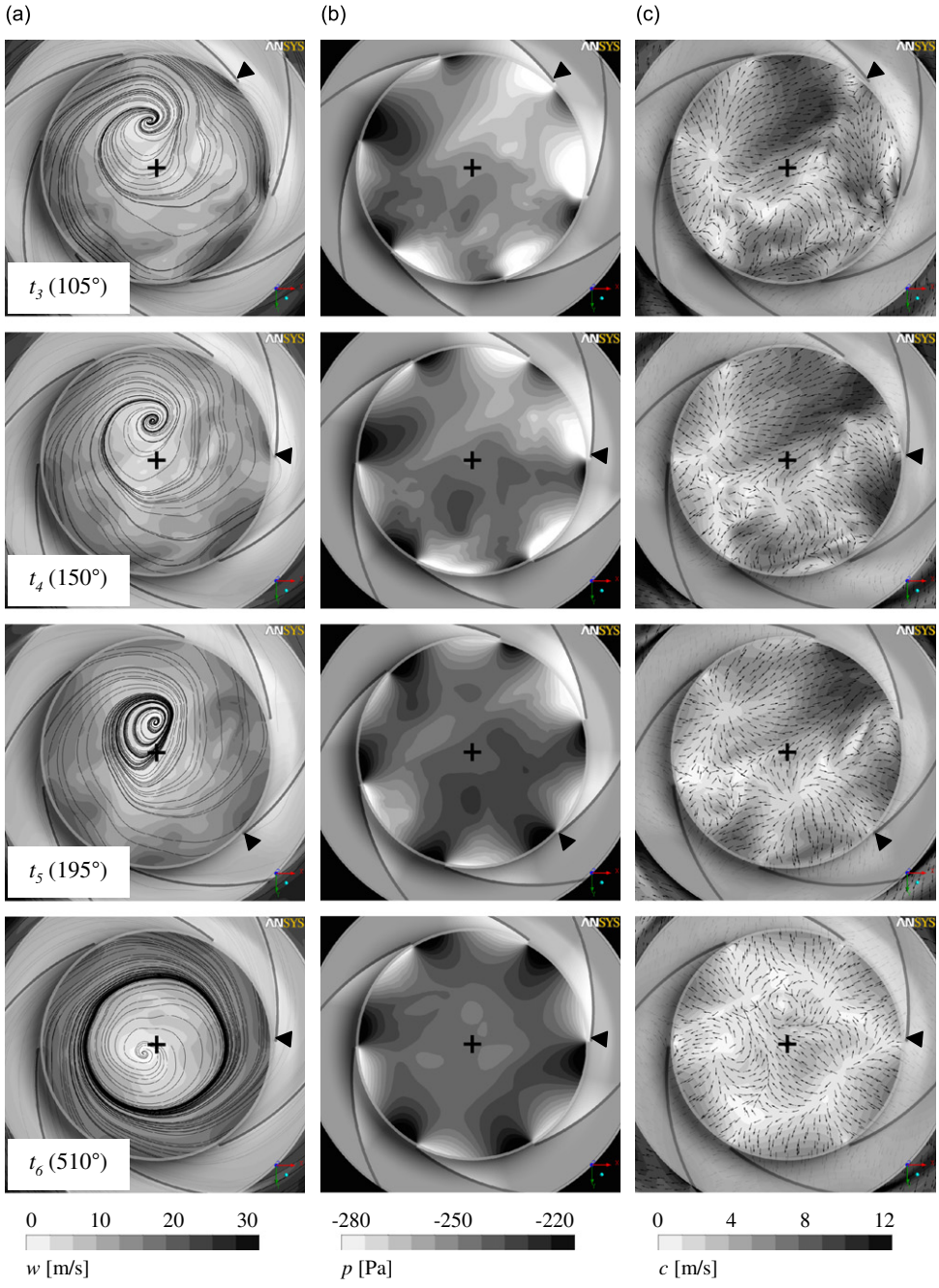

Fig. 21. Time series of the instantaneous flow field at an axial position ξ_{11}=0.95 in the intake: (a) streamlines of relative flow velocity, (b) static pressure distribution, and (c) vectors of absolute flow velocity (center of impeller indicated by +).

favourably, while amplitude shows some differences. Nevertheless, the numerical prediction seemingly represents the key phenomenon in the intake flow field. Further validation of the numerical results was obtained by averaging pressures at the intake and discharge with respect to space and time. Overall impeller pressure rise as predicted by the numerical simulation is very close to measurements (Fig. 6).

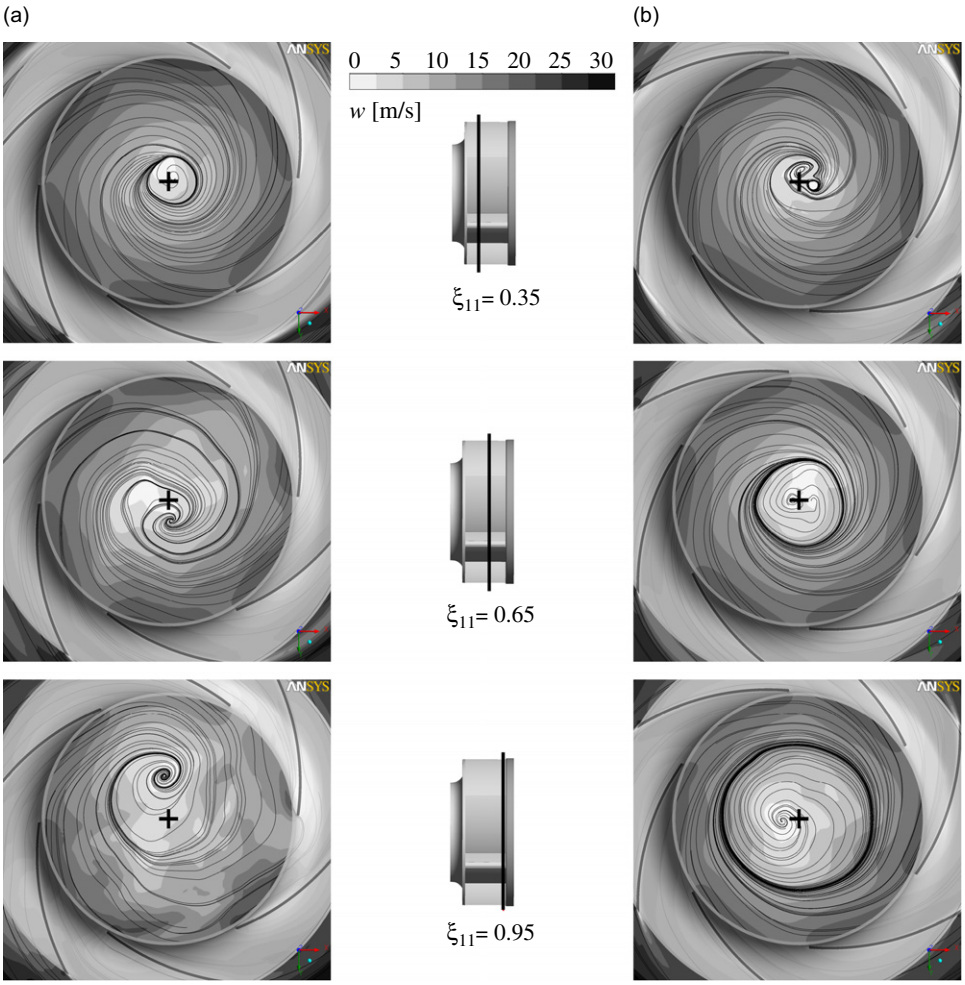

Fig. 22. Instantaneous flow field as a function of axial position in the intake: (a) at t_4 and (b) at t_6.

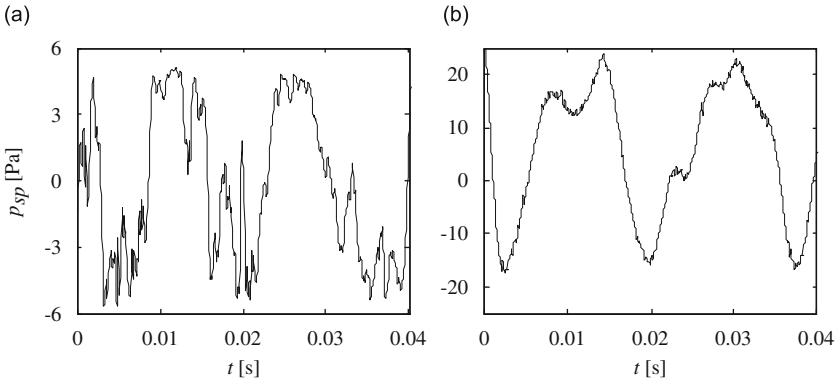

Fig. 23. Time record of blade surface pressure fluctuation at monitoring point ξ_{11}=0.9, ξ_3=0.03: (a) measurement and (b) numerical prediction.

6. Summary and conclusion

As in any centrifugal impeller the fluid at the intake is deflected from a purely axial to a radial direction. This does not happen abruptly as the fluid passes the blade leading edges. The blades and friction of the rotating hub gradually impose a pre-swirl on the inflow and cause the formation of an inlet vortex. A key result of this study is that in the impellers investigated this inlet vortex is not stable. It takes a helical form, with the vortex core slowly varying its position with respect to the impeller center. Also vortex strength varies with time. Characteristic frequencies associated with the vortex movement are very small as compared with blade speed. In fact, the vortex structure can be considered as being nearly stationary for small time intervals. Thus, the blades cut through the quasi-stationary helical vortex each time it meets a trailing edge. This is the reason for strong blade surface pressure and hence force fluctuations, which eventually act as sources for tones produced at BPF. On the other hand slow spin of the vortex core and slow variation of vortex strength are responsible for amplitude modulation of the BPF tone as observed and clearly audible in the experiments.

Reducing the tonal noise at blade passing frequency and its higher harmonics would require a design that is substantially free from an unstable inlet vortex. Much current knowledge of stability of swirling flows is based on studies in pipes. Stability criterions are the ratio of axial to circumferential flow velocity and its radial distributions. However, the formation of the vortex in the intake of a centrifugal impeller is seemingly more complex. Chen et al. [25] refer to an inlet vortex, but due to inlet guide vanes. More likely the vortex structure detected here is related to the draft tube vortex found in water turbines or in the intake of pumps [26]. Further effort is required to link geometric design parameters such as intake or width to impeller diameter ratio and aerodynamic non-dimensional coefficients to the existence of a stable or unstable inflow, which, in consequence, is essential for a low noise fan design.

Acknowledgements

This investigation was partly funded by the German Federal Ministry of Economics and Technology (BMWi) via the consortium for industrial research "Otto von Guericke" (AiF) under Grant 14611N/1 and the Forschungsvereinigung Luft- und Trocknungstechnik e.V. (FLT). The authors gratefully acknowledge this support. We would also like to thank the German–American Fulbright Commission, which supported two sabbatical leaves of the coauthor at the Pennsylvania State University (PSU), USA. The collaboration with D.K. McLaughlin from the Aerospace Department at PSU was helpful in many aspects. The authors express their appreciation to Dr. Hauke Reese, now with Fluent Deutschland, who assisted in setting up the unsteady computational fluid dynamics computations.

References

[1] K.-R. Fehse, W. Neise, Generation mechanisms of low-frequency centrifugal fan noise, AIAA-Paper AIAA-98-2370, 1998.
[2] J.-S. Choi, D.K. McLaughlin, D.E. Thompson, Experiments on the unsteady flow field and noise generation in a centrifugal pump impeller, *Journal of Sound and Vibration* 263 (2003) 493–514.
[3] M. Gottschalk , Untersuchung der Kennlinienstetigkeit von Radialventilatoren (Investigation of discontinuous performance curves of centrifugal fans), Strömungsmechanik und Strömungsmaschinen, Heft 17 September 1974, Verlag G. Braun Karlsruhe, 1974.
[4] L. Mongeau, D.E. Thompson, D.K. McLaughlin, Sound generation by rotating stall in centrifugal turbomachines, *Journal of Sound and Vibration* 163 (1) (1993) 1–30.
[5] L. Mongeau, D.E. Thompson, D.K. McLaughlin, A method for characterizing aerodynamic sound sources in turbomachines, *Journal of Sound and Vibration* 181 (3) (1995) 369–389.
[6] L.G. Tetu, D.K. McLaughlin, D.E. Thompson, Noise produced by large scale instability modes in centrifugal turbomachinery, *Proceedings of the ASME Noise Control and Acoustics Division*, NCA-vol. 21, 1995.
[7] P. Fringe, R. Van den Braembussche, A theoretical model for rotating stall in the vaneless diffuser of a centrifugal compressor, *Journal of Engineering for Gas Turbines and Power* 107 (1985) 507–513.
[8] G. Pavesi, G. Cavazzani, G. Ardizzon, Time–frequency characterization of the unsteady phenomena in a centrifugal pump, *International Journal of Heat and Fluid Flow* 29 (2008) 1527–1540.
[9] T. Carolus, D.K. McLaughlin, R. Basile, Experimental investigation of the unsteady discharge flow field and the noise of a centrifugal fan impeller, *Proceedings of the Seventh International Congress on Sound and Vibration*, Garmisch-Partenkirchen, Germany, 2000.
[10] D. Wolfram, Th. Carolus, Akustische Quellen bei gehäuselosen Radialventilatoren: analyse, Modelle, Minderung (Acoustic sources in isolated centrifugal fans: analysis, models, reduction), Report No. F20910A, Institut für Fluid- und Thermodynamik, Universität Siegen, 2009.
[11] Deutsche Gebrauchsmusterschrift, Radialventilator und Düse für einen Radialventilator (Centrifugal fan and inlet nozzle), DE 200 01 746 U 1, June 21, 2001.
[12] M.V. Lowson, The sound field for singularities in motion. *Proceedings of the Royal Society*, London, A 286 (559–572), 1965.
[13] S.E. Wright, The acoustic spectrum of axial flow machines, *Journal of Sound and Vibration* 45 (1976) 165–223.
[14] M. Roger, Noise in Turbomachines—noise from moving surfaces, in: VKI-Lecture Series 2000–02, von Karman Institute for Fluid Dynamics, Belgium, 2000.
[15] M.E. Goldstein, *Aeroacoustics*, McGraw-Hill, 1974.
[16] W.K. Blake, *Mechanics of Flow Induced Sound and Vibration*, Academic Press Inc., 1986.
[17] DIN 24163, Ventilatoren, Teil 2: Leistungsmessung—Normprüfstände (Fans, part 2: performance tests—standardized test rigs), Deutsche Norm, 1985.
[18] J. Weidemann, Beitrag zur Analyse der Beziehungen zwischen den akustischen und strömungstechnischen Parametern am Beispiel geometrisch ähnlicher Radialventilator-Laufräder (A contribution to the analysis of the relationship between acoustic and aerodynamic parameters for geometrically similar centrifugal fan impellers), DLR-Forschungsbericht 12-71, 1971.
[19] P.H. Bent, Experiments on the aerodynamic generation of noise in centrifugal turbomachinery, Ph.D. Thesis, Pennsylvania State University, 1993.
[20] L.G. Tetu, D.K. McLaughlin, D.E. Thompson, Noise produced by large scale instability modes in centrifugal turbomachinery, *Proceedings of the ASME Noise Control and Acoustics Division*, NCA-vol. 21, 1995.

[21] J.S. Bendat, A.G. Piersol, *Engineering Applications of Correlation and Spectral Analysis*, John Wiley & Sons, Inc., 1993.
[22] D. Wolfram, Analyse des Entstehungsmechanismus von Drehtönen bei gehäuselosen Radialventilatoren (Analysis of the blade passing frequency tone mechanism in isolated centrifugal fan impellers). Fortschritt-Bericht VDI Reihe 7 Nr. 496, VDI-Verlag, 2009.
[23] F.R. Menter, M. Kuntz, R. Bender, A scale adaptive simulation model for turbulent flow predictions, AIAA Paper AIAA2003-0767, 2003.
[24] F.R. Menter, Y. Egorov, A scale-adaptive simulation model using two-equation models. AIAA Paper AIAA2005-1095, 2005.
[25] P. Chen, M. Soundra-Nayagan, H.C. Simpson, Unstable flows in centrifugal fans, *Proceedings of IMechE 1992–3*, 1992, pp. 25–32.
[26] J.F. Gülich, Kreiselpumpen, Springer-Verlag, 2nd ed., 2004.